Chapter 11

WiFi CSI-based vital signs monitoring

Daqing Zhang[a], Youwei Zeng[a], Fusang Zhang[a], and Jie Xiong[b]

[a]*School of Electronics Engineering and Computer Science, Peking University, Beijing, China,*
[b]*College of Information and Computer Sciences, University of Massachusetts, Amherst, Amherst, MA, United States*

Contents

11.1 Introduction

Respiration monitoring plays a critical role in daily health care. Long-term respiration monitoring is widely used to track the progression of illness and also to predict emergencies that require immediate clinical attention, such as cardiac arrest [1]. Among many technologies employed for respiration monitoring, WiFi-based solutions have emerged in recent years due to the pervasive deployment of WiFi infrastructure at home and in public areas. The intrinsic nature of sensor-free and contact-free makes WiFi-based solutions particularly appealing in the current COVID-19 pandemic scenarios as compared to traditional sensor-based solutions.

The rational behind WiFi-based respiration monitoring is that the WiFi receiver (e.g., mobile phone, laptop, etc) captures the WiFi signal reflected off the human body, which contains the subtle displacement information caused by human respiration. The signal waveform varies with the exhalation and inhalation process periodically, and the respiration information can thus be extracted by analyzing the WiFi signal variation. Based on this basic idea, Liu et al. [2] explore the feasibility of employing WiFi signals to detect human respiration. Soon after that, in 2016, Wang et al. [3] found that the performance of WiFi-based respiration sensing is not always stable and is highly dependent on target location and orientation. This work triggered the following research to not just focus on sensing accuracy but also on robustness and practicality. Subsequent work [4,5] investigates the sensing stability and sensing range to further enhance the performance.

In this chapter, we first review the history of WiFi-based respiration monitoring and then introduce the theoretical models to help people to deeply understand the underlying mechanisms of WiFi sensing. The state-of-the-art solutions proposed to address the instability and limited range issues are introduced by taking human respiration monitoring as an example application. Finally, we present the approach to enable multi-person vital signs monitoring, which we believe is an important step towards real-life adoption of WiFi-based respiration monitoring.

11.2   An historic review of WiFi-based human respiration monitoring

11.2.1   RSS-based respiration monitoring

The Received Signal Strength (RSS) characterizes the attenuation of RF signals during the propagation process, and RSS readings are widely available on mainstream commodity hardware. The pioneer work [6] studying the feasibility of employing RSS signals for respiration monitoring was proposed in 2013. It makes use of links formed by a mesh network of multiple IEEE 802.15.4 nodes to estimate the respiration rate of a single person in the environment [6]. Later, in 2014, a more cost-effective solution was developed by O.J. Kaltiokallio et al. [7] in which only one pair of Zigbee nodes was required to monitor the respiration rate. In 2015, Abdelnasser et al. successfully realized respiration monitoring using commodity WiFi hardware [8]. Though promising, several issues were also pointed out including the coarse resolution and severe hardware noise. Therefore, the performance of the RSS-based solutions is limited in terms of accuracy and stability.

11.2.2   CSI-based respiration monitoring

One exciting opportunity emerged when the 802.11n WiFi standard was officially released in 2009 [9]. To support the multiple-input and multiple-

output (MIMO) feature of 802.11n, channel state information (CSI) became available on commodity WiFi hardware. Soon thereafter, in 2011, the CSI tool [10] was developed to retrieve CSI readings from an Intel 5300 network interface card (NIC). Compared to RSS, CSI readings have the unique advantage of finer resolution and lower noise, and therefore, the sensing granularity and performance stability are significantly improved. Furthermore, RSS contains just the signal amplitude, but CSI contains amplitude and phase information, which can both be utilized for respiration monitoring.

Wi-Sleep [11] was among the first systems that can extract rhythmic respiration patterns from WiFi-CSI signals. In 2015, Liu et al. [12] claimed to monitor not just the respiration rate but also the heartbeat rate during sleep by analyzing the power spectral density (PSD) of CSI amplitude. Wu et al. [13] further extended respiration monitoring from sleeping to standing postures. While interesting progress had been achieved, researchers also found one critical issue with respiration monitoring: The performance is unstable and at certain locations (i.e., the "blind spots"), e.g., the performance can severely degrade even when the target is close to the WiFi transceivers. During the time period 2016–2018, the Fresnel zone models were introduced by the Peking University team in [3,14–16] to explain the underlying mechanism of WiFi-based respiration sensing. The Fresnel zone models mathematically characterize the relationship between the human chest displacements and the corresponding signal variations. People can therefore rely on these models to fully understand why the "blind spots" occur and propose solutions [4,5,17] to address this issue.

Leveraging the overlapped Fresnel zone model, Wang et al. [18] employed multiple transceiver pairs to overcome the blind-spot issue. In 2018, Zeng et al. discovered that the phase and amplitude are complementary to each other for respiration monitoring [4]. That is to say, when the sensing performance is bad using phase, it would be good with amplitude and vice versa. Therefore, amplitude and phase can be employed together to remove sensing "blind spots". Another interesting solution was proposed by Niu et al. [17] in 2018, who proposed to add a man-made "virtual" multipath to boost the respiration sensing performance at the "blind spots" to address the issue.

In addition to sensing respiration for one person, an exciting research direction in this area is to enable multi-target respiration monitoring. Different from traditional sensor-based solutions in which multi-target sensing is not an issue, it is very challenging to achieve multi-target respiration monitoring with WiFi because the reflection signals from multiple targets can be mixed at the receiver, and it is difficult to separate them to obtain the respiratory information of each individual. Liu et al. [12] presented the first attempt in this direction and demonstrated the feasibility of multi-person respiration monitoring by applying Fast Fourier Transform (FFT) on the CSI amplitude readings. Wang et al. [19] achieved multi-person respiration monitoring by applying the root-MUSIC algorithm [20] on the CSI phase readings. A similar method was also adopted in TR-BREATH [21] to achieve multi-target respiration monitoring. Wang et

al. [22] further leveraged the tensor decomposition technique to extract the respiration patterns of multiple targets from the CSI phase readings. Though promising, one basic assumption for the aforementioned systems to work is that the respiration rates of different persons are distinct, and the performance degrades when different people have similar respiration rates. Furthermore, these systems can only obtain the average respiration rate over a period of time but are not able to extract the detailed respiration pattern over time. Inspired by the Fresnel zone theories [3,14–16], Yang et al. [23] successfully managed to monitor multi-person respiration by optimizing the deployment of WiFi transceivers so that each transceiver pair's transmission is only affected by one target. However, this method requires knowing the accurate location of each target in advance, and if the target changes the location, the deployment stops working and needs to be updated. In 2020, by leveraging the widely available antenna array with commodity WiFi hardware, Zeng et al. [24] proposed to model the multi-person respiration sensing as a BSS (Blind Source Separation) problem and solved it using the independent component analysis (ICA) method to separate and extract the respiration information of each individual person; even multiple targets have similar respiration rates and are physically closely located.

Besides respiration sensing for multiple subjects, another important research direction in this area is to increase the sensing range. Due to the nature of employing weak reflection signals for respiration sensing, the WiFi sensing range is very limited, being much smaller than the communication range. In 2019, Zeng et al. [5] pushed the respiration sensing range from room level (two–four m) to house level (eight–nine m) by introducing a new metric called the CSI ratio, which is defined as the ratio of CSI readings collected from two co-located antennas hosted on the same Wi-i hardware. With an increased sensing range, through-wall respiration sensing was also demonstrated with WiFi signals [5].

Other attempts in this area include [25,26] and [27]. By synthesizing a wider-bandwidth WiFi radio, Shi et al. [25] demonstrated they can detect a person's respiration rate in dynamic ambient environment. With the synthesized WiFi signal, the authors can identify the path reflected by the breathing person and then analyze the periodicity of the signal-power measurements only from this path to infer the respiration rate. Zhang et al. [26] calibrated the time-varying phase offset by using cables and splitters, and then it exploited the variation of accurate CSI phase to track human breath. One interesting observation worth mentioning is that, by comparing the respiration monitoring performance using different RF signals including WiFi RSS, Zigbee RSS, WiFi CSI, and UWB-IR [27], Hillyard et al. found that WiFi-CSI readings presented the most robust respiration monitoring performance.

With significant progress in this area, accurate and robust WiFi respiration monitoring has become a reality. However, challenges still exist. For example, while monitoring the respiration rate of a sleeping person is not an issue anymore, monitoring the respiration of a person running on a treadmill remains challenging due to the large self-interference movements from other body parts.

Severe interference from surrounding people is another critical issue that needs to be tackled before WiFi-based respiration monitoring can be widely adopted in real life.

11.3 The principle of WiFi CSI-based respiration monitoring

11.3.1 The basics of WiFi CSI

Due to reflection, diffraction, and scattering from surrounding objects, wireless signals (e.g., WiFi) arrive at the receiver from the transmitter through multiple paths. Channel State Information (CSI) is used to quantify the wireless propagation channel between the transmit–receive (Tx-Rx) pair. In essence, CSI characterizes the *Channel Frequency Response* (CFR) of each subcarrier between each antenna pair. For carrier frequency f, $X(f,t)$ and $Y(f,t)$ are the frequency domain representations of the transmitted and received signals, respectively. Letting $H(f,t)$ be the complex-valued CFR for carrier frequency f measured at time t, we have the relationship $Y(f,t) = H(f,t) \times X(f,t)$ [28]. As CSI on WiFi hardware is measured on each OFDM subcarrier, one CSI measurement is a CFR value between an antenna pair on a certain OFDM subcarrier frequency at a particular time stamp.

If an RF signal arrives at the receiver through L different paths, then the total CSI is the linear superposition of the CSI of all paths, which can be represented as:

$$H(f,t) = \delta(t)e^{-j\phi(t)} \sum_{i=1}^{L} A_i e^{-j \cdot 2\pi d_i(t)/\lambda}, \tag{11.1}$$

where $\delta(t)$ is the amplitude impulse noise, $\phi(t)$ is time-varying phase shift, L is the number of paths, A_i is the complex attenuation, and $d_i(t)$ is the signal propagation length of the ith path.

11.3.2 Modeling human respiration

The respiration process of a person consists of periodic inflation and deflation of the lungs as shown in Fig. 11.1. The chest displacement during respiration is around 4.2–5.4 mm in the front dimension, 2.5–2.6 mm in the back dimension, and 0.6–1.1 mm in the mediolateral dimension. For a deep inspiratory breath hold (DIBH), this displacement can be increased up to 12.6 mm in anteroposterior dimension [29]. We model the human chest as a varying size flat-cylinder, as shown in Fig. 11.2, where the outer and inner cylinder surfaces correspond to the chest positions for exhalation and inhalation, respectively.

11.3.3 Fresnel diffraction and reflection sensing models

In this section, we quantify the relationship between the human chest motion and the variation of WiFi CSI by employing the Fresnel diffraction and reflection
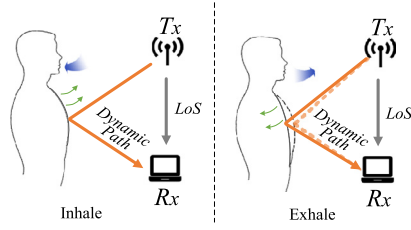
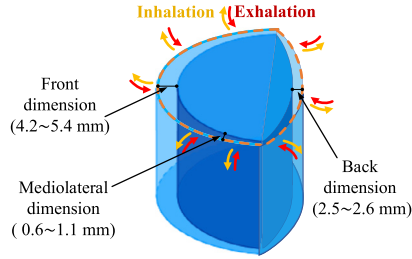**FIGURE 11.1** An example of how RF signal paths change with body chest motions during the respiration process.
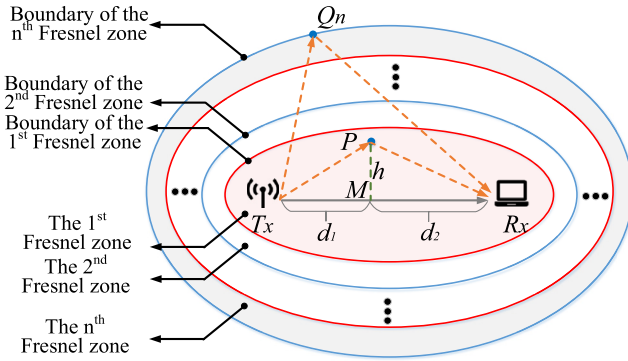

FIGURE 11.2 Human chest modeling.

FIGURE 11.3 Geometry of the Fresnel zones.

sensing models. In free space, Fresnel zones are concentric ellipses with the transmitter T_x and receiver R_x as two focal points. The innermost ellipse is the called the First Fresnel Zone (FFZ), and more than 70% of the signal energy is transferred to the receiver via this zone. The nth Fresnel zone corresponds to the area between the $(n-1)^{th}$ and n^{th} ellipses. For a given RF wavelength λ, the Fresnel zones can be represented as follows:

$$|T_x Q_n| + |Q_n R_x| - |T_x R_x| = n\lambda/2, \qquad (11.2)$$

where Q_n is a point on the nth ellipse. When a point P is inside the FFZ, the distance from P to the line-of-sight (LoS) path formed by the transceiver pair is h, as shown in Fig. 11.3. M is the intersection point of the vertical line and the LoS path. The path $T_x R_x$ is then divided into two segments: $d_1 = |T_x M|$ and $d_2 = |M R_x|$. The path difference Δd between the path $T_x P R_x$ and the LoS path $T_x R_x$ is calculated by:

$$\begin{aligned} \Delta d &= |T_x P| + |P R_x| - |T_x R_x| \\ &= \sqrt{(d_1)^2 + (h^2)} + \sqrt{(d_2)^2 + (h^2)} - (d_1 + d_2) \\ &= d_1 \sqrt{1 + (h/d_1)^2} + d_2 \sqrt{1 + (h/d_2)^2} - (d_1 + d_2). \end{aligned} \tag{11.3}$$

This path difference can be used to derive the phase difference between the target reflection path and the direct LoS path as the following:

$$\varphi = \frac{2\pi \, \Delta d}{\lambda}. \tag{11.4}$$

When the human target is located outside of the FFZ, reflection dominates. On the other hand, when the target is inside the FFZ, diffraction dominates. We discuss the effects of diffraction and reflection, respectively, next.

Diffraction effect: When the target P is located inside the FFZ, we have $h \ll d_1$ and $h \ll d_2$. Therefore, $(h/d_1)^2 \ll 1$ and $(h/d_2)^2 \ll 1$. By applying the approximation $\sqrt{1 + x} \approx 1 + \frac{x}{2}$ when $x \ll 1$, Eq. (11.3) can be simplified as:

$$\Delta d \approx \frac{h^2}{2} \frac{(d_1 + d_2)}{d_1 d_2}. \tag{11.5}$$

The corresponding phase difference induced by this path-length difference Δd can then be expressed as:

$$\varphi = \frac{2\pi \, \Delta d}{\lambda} = \pi h^2 \frac{(d_1 + d_2)}{\lambda d_1 d_2}. \tag{11.6}$$

The Fresnel diffraction parameter v is defined as follows:

$$v = h \sqrt{\frac{2(d_1 + d_2)}{\lambda d_1 d_2}} = \sqrt{\frac{2}{\pi} \varphi}. \tag{11.7}$$

With this parameter, the signal amplitude at the receiver due to diffraction can be expressed as [30]:

$$F(v) = \frac{1 + j}{2} \cdot \int_v^\infty exp(\frac{-j\pi z^2}{2}) dz, \tag{11.8}$$

where $F(v)$ is known as the Fresnel integral. The diffraction gain induced by the target P can thus be expressed as:

$$Gain_{Dif} = 20log|F(v)|. \qquad (11.9)$$

Reflection effect: When the target P is located outside of the FFZ, reflection dominates. The reflection signal at the receiver is a superposition of both static path and dynamic path signals. In the respiration monitoring scenario, the signal reflected from a surrounding wall is a static path signal, while the signal reflected from the human chest is a dynamic path signal. The received signal can then be denoted as:

$$H(t) = H_s + H_d(t) = H_s + A(t)\exp\left(-j\frac{2\pi \Delta d}{\lambda}\right), \qquad (11.10)$$

where the static component H_s is the sum of static path signals and the dynamic component $H_d(t)$ is induced by the moving human chest. $A(t)$ is the complex-valued representation of the signal amplitude and phase of the dynamic path, and $e^{-j2\pi\frac{\Delta d}{\lambda}}$ is the phase change caused by the length change of the dynamic path. Note that, when the length of the reflected signal path changes by λ, its phase rotates 2π. Hence the receiving signal $H(t)$ has a time-varying signal amplitude whose power can be represented as:

$$|H(\theta)|^2 = |H_s|^2 + |H_d|^2 + 2|H_s||H_d|\cos\theta, \qquad (11.11)$$

where θ is the phase difference between the static signal H_s and dynamic vector H_d. Based on this formula, we know that when an object crosses the Fresnel zone boundaries, the amplitude of the receiving signal varies like a sinusoidal wave.

To demonstrate this effect, we let a cylinder move across multiple Fresnel zone boundaries as shown in Fig. 11.4. According to the diffraction and reflection models [3,16], we plot the amplitude of the received signal. When the cylinder is located outside of the FFZ, the signal amplitude varies like a sinusoidal wave. The signal amplitude varies in the shape of a "W" during the process of crossing the FFZ.

Now, we explain why a subtle human chest displacement during the respiration process can cause such a large signal variation. If the chest displacement is 0.5 cm, for the wavelength (λ) of 5.7 cm, the corresponding phase change of the signal path during the process is around $63°$ ($2\pi \times \frac{2\Delta d}{\lambda} = 2\pi \times \frac{2\times0.5}{5.7} = 63°$). Note that the resultant signal received at the receiver is a superposition of both static and dynamic signals. For a same amount of phase variation ($63°$) of the dynamic signal, the amount of signal variation of the resultant signal depends on the location of the target. We choose four different locations and let a cylinder vibrate with a small displacement at these locations to mimic the respiration of a person. As shown in Fig. 11.5, at Location 1, the cylinder vibration leads to a small signal-amplitude variation, and each respiration cycle
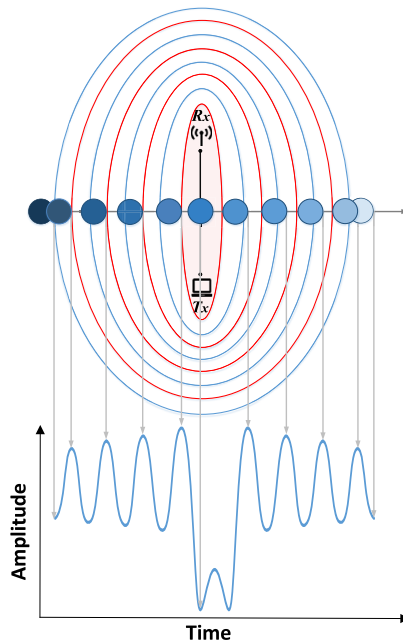
FIGURE 11.4 Amplitude changes of the resultant signal while the target moves across the Fresnel zones.
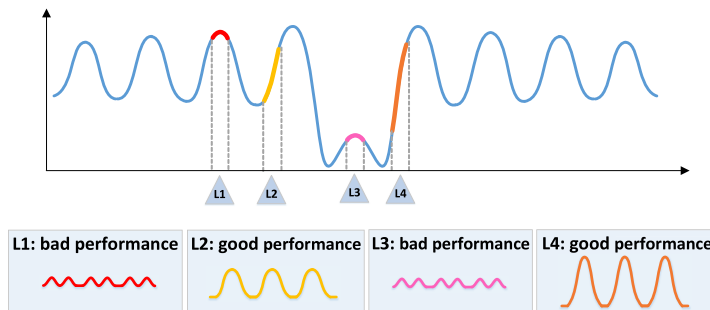

FIGURE 11.5 Amplitude of the resultant receiving signal for various target locations.

corresponds to two peaks. At Location 2, the same cylinder vibration leads to a much larger signal-amplitude variation, and each respiration corresponds to just one peak. For respiration monitoring, a better performance can be achieved at Location 2 because a clearer respiration pattern can be obtained. Similarly, bad and good performance can be achieved at Location 3 and Location 4 respectively.
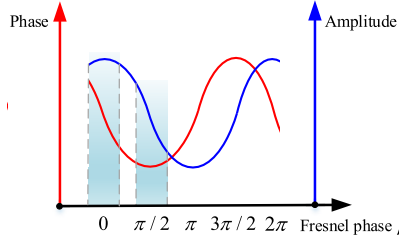
FIGURE 11.6 CSI phase and amplitude waveforms with respect to various target locations.

11.4 Robust single-person respiration monitoring

In this section, we focus on single-person respiration monitoring and present the state-of-the-art solutions to address the two issues discussed in Sect. 11.3: (i) the "blind spot" issue and (ii) short sensing range.

11.4.1 Removing "blind spots" for respiration monitoring

We present two methods to address the "blind spot" issue: (i) exploiting the complementarity of CSI amplitude and phase to ensure respiration monitoring performance; (ii) adding a "virtual" multipath to ensure large signal variation.

11.4.1.1 Exploiting complementarity of CSI amplitude and phase
Based on Eq. (11.10), the phase of CSI reading can be denoted as [4]:

$$\angle H_s - \arcsin \frac{|H_d| \sin \rho}{\sqrt{|H_s|^2 + |H_d|^2 + 2|H_s||H_d| \cos \rho}}, \qquad (11.12)$$

where ρ is the Fresnel phase, which is defined as the phase difference between the dynamic signal vector H_d and static signal vector H_s. Mathematically, the CSI phase in Eq. (11.12) changes in the form of a sinusoidal-like wave.

Based on the definition of CSI phase and amplitude, we conduct simulations and plot the ideal CSI phase and amplitude waveforms in Fig. 11.6. We observe that, the CSI phase changes very little in the middle of a Fresnel zone (e.g., $\rho = \pi/2$ and $3\pi/2$), but more significantly at the boundary of a Fresnel zone (e.g., $\rho = 0, \pi$ and 2π). This suggests that, when CSI phase is employed for respiration sensing, the best subject location would be right at the boundary of a Fresnel zone and the worst location would be in the middle of a Fresnel zone. Interestingly, we observe that a bad location for sensing with amplitude turns out to be a good position for sensing with phase, and vice versa as shown in Fig. 11.6.

However, the CSI measurement in commodity WiFi suffers from the time-varying phase offset, which makes phase readings totally random across consecutive CSI samples. Fortunately, the time-varying random phase offsets are
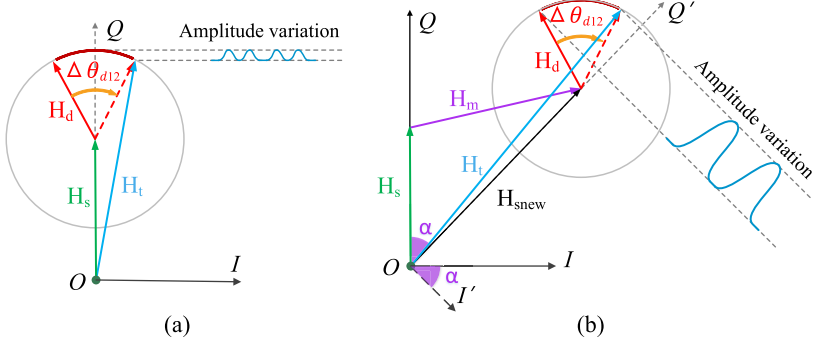
FIGURE 11.7 The effect of adding a multipath: (a) without a multipath; (b) with a multipath.

the same at different antennas on one WiFi card [31] since they share the same RF oscillator. Thus, we can apply conjugate multiplication of CSI between two antennas to remove the random phase offset. After the phase offset is removed, clean phase readings are obtained. Then, both phase and amplitude readings can be employed for respiration sensing. The complementary property between phase and amplitude in terms of sensing performance helps to ensure reliable human respiration monitoring without "blind spots".

11.4.1.2 Adding 'a 'virtual" multipath

Instead of eliminating the "blind spots" by combining both amplitude and phase for sensing, a novel method was proposed to significantly boost the respiration sensing performance at the "blind spots" by adding a man-made "virtual" multipath [17]. From the previous subsection, we know the Fresnel phase ρ (i.e., the phase difference between the dynamic and static component) is the key factor affecting the sensing performance. Therefore, we propose to a leverage multipath, which is commonly considered harmful in the existing sensing literature, to tune the phase of the static component for better sensing performance.

As shown in Fig. 11.7, when a new static multipath is introduced, the original static component H_s and the new multipath component H_m together form a new static component H_{snew}. The dynamic vector H_d is not changed but now rotates around the new static vector H_{snew}. From the perspective of vector transformation, adding such a multipath actually transforms the original IQ vector space to a new I'Q' vector space as shown in Fig. 11.7(b). After introducing a static virtual multipath, the original static vector H_s is converted to the new static vector H_{snew}, making the variation of the dynamic vector more distinguishable. With this multipath added, we successfully turn a "bad" position into a "good" position for sensing. That is to say, we can create a static multipath to improve the sensing performance at a particular location. In practice, we can either employ a physical object to create a multipath or add a "virtual" multipath value purely in software.
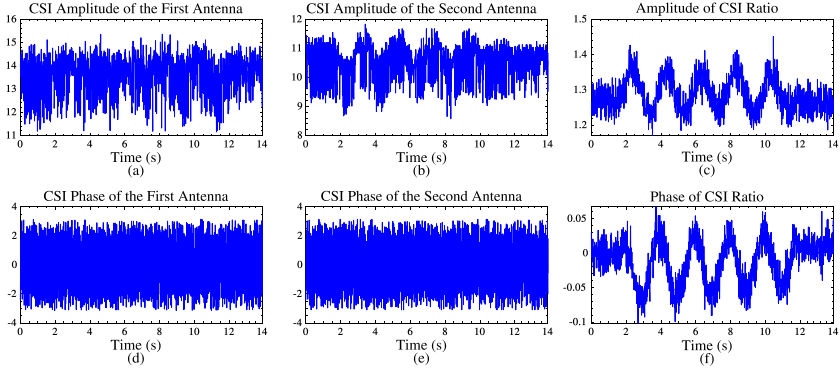
FIGURE 11.8 Comparison of raw CSI and CSI ratios when they are employed to sense the plate movements.

11.4.2 Pushing the sensing range of respiration monitoring

In this subsection, we aim to increase the respiration sensing range by constructing a new base signal called the CSI ratio.

11.4.2.1 The CSI-ratio model

The CSI ratio is defined as the quotient of CSI readings between two antennas of a receiver as:

$$
\begin{aligned}
H_{ratio}(f,t) &= \frac{H_1(f,t)}{H_2(f,t)} \\
&= \frac{\delta(t)e^{-j\phi(t)}(H_{s,1} + A_1 e^{-j2\pi d_1(t)/\lambda})}{\delta(t)e^{-j\phi(t)}(H_{s,2} + A_2 e^{-j2\pi d_2(t)/\lambda})} \\
&= \frac{H_{s,1} + A_1 e^{-j2\pi d_1(t)/\lambda}}{H_{s,2} + A_2 e^{-j2\pi d_2(t)/\lambda}},
\end{aligned}
\tag{11.13}
$$

where $H_1(f,t)$ is the complex-valued CSI of the first antenna and $H_2(f,t)$ is that of the second antenna. With the division operation, it can be seen that the noise in the original CSI amplitude and the time-varying phase offset are successfully canceled out, thus providing a high-SNR new base signal for sensing. Fig. 11.8 presents an example of sensing the plate movement to visualize the effect of noise cancellation with CSI ratio. Apparently, the CSI ratio of two antennas eliminates the noise but still retains the signal variation pattern corresponding to the plate movements.

Now let us take a deeper look at how to utilize the CSI ratio for human sensing. Prior work presents an interesting observation: When the target moves a short distance, although the target-reflection path length at each antenna changes, the target-reflection path-length difference between two close-by antennas $d_2(t) - d_1(t)$ can be seen as a constant [4]. With this observation,

Eq. (11.13) can be rewritten as:

$$
\begin{aligned}
H_{ratio}(f,t) &= \frac{A_1 e^{-j2\pi d_1(t)/\lambda} + H_{s,1}}{(A_2 e^{-j2\pi(d_2(t)-d_1(t))/\lambda}) e^{-j2\pi d_1(t)/\lambda} + H_{s,2}} \\
&= \frac{\mathcal{A}\mathcal{Z} + \mathcal{B}}{\mathcal{C}\mathcal{Z} + \mathcal{D}},
\end{aligned}
\tag{11.14}
$$

where the coefficient $\mathcal{A}, \mathcal{B}, \mathcal{C}, \mathcal{D}$ are complex constants, and $\mathcal{Z} = e^{-j2\pi d_1(t)/\lambda}$ is a unit complex variable, whose phase is closely related to the reflection path length. Mathematically, Eq. (11.14) is exactly in the form of a Möbius Transformation (also known as fractional transformation) [32]. To study the properties of CSI ratio, we rewrite Eq. (11.14) as:

$$
\begin{aligned}
H_{ratio}(f,t) &= \left(\frac{\mathcal{B}\mathcal{C} - \mathcal{A}\mathcal{D}}{\mathcal{C}^2} \right) \frac{1}{\mathcal{Z} + \mathcal{D}/\mathcal{C}} + \frac{\mathcal{A}}{\mathcal{C}} \\
&= \frac{\beta e^{j\theta}}{\mathcal{Z} + \alpha} + \gamma,
\end{aligned}
\tag{11.15}
$$

where α and γ are complex numbers; β and θ are real numbers. We can see from Eq. (11.15) that the Möbius transformation can be decomposed into four basic operations, namely, translation, rotation, scaling, and inversion. The translation, rotation, and scaling preserve the geometry shape and rotation direction (clockwise or counterclockwise) of a circle. The inversion operation preserves the shape of a circle, however, it may change the rotational direction [5]. When the magnitude of the static component is larger than that of the dynamic component (i.e., $|\mathcal{D}| > |\mathcal{C}|$), which is usually the case in human sensing [5], the inversion operation still preserves the rotational direction.

Through rigorous mathematical derivation and real-life experiments in [5], we can obtain the following properties for human sensing from the CSI-ratio model in Eq. (11.14):

1. The CSI ratio preserves the relationship between target movements and the corresponding CSI changes. Specifically, if the reflection path length is changed by one wavelength, due to target movement, the CSI ratio would rotate for a full circle in the complex plane. If the path length is changed by less than one wavelength, the CSI ratio just rotates a small part (an arc) along the circle.
2. If the reflection path length increases, CSI ratio rotates clockwise when the magnitude of the static component is larger than that of the dynamic component. If the path length decreases, CSI ratio rotates counterclockwise.
3. The amplitude and phase of the CSI ratio is complementary to each other for respiration sensing.
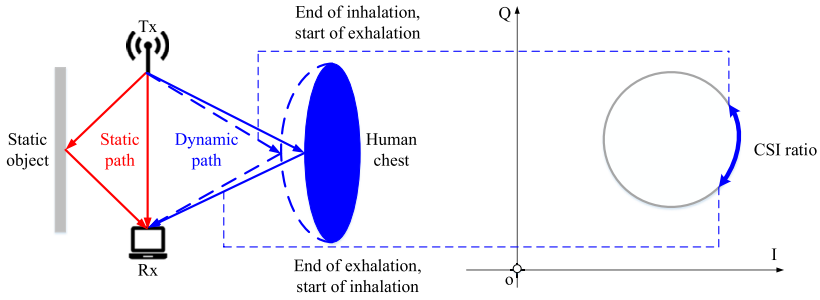
FIGURE 11.9 Conceptual illustration of applying CSI ratio to sense single-person respiration.
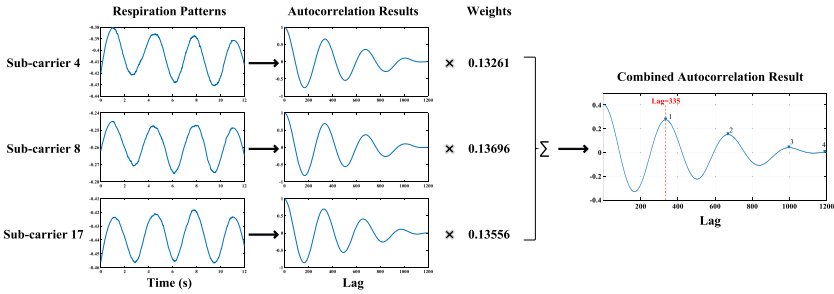

FIGURE 11.10 Example of multiple sub-carriers combining. In this case, we use the weighted sum of three selected sub-carriers' autocorrelation results to obtain a final one. The estimated respiration rate is $\frac{60}{335/100} = 17.9$ bpm.

11.4.2.2 Applying CSI ratio to single-person respiration sensing

Since the chest displacement caused by respiration is between 0.6 mm to 12.6 mm, the reflection path length changes less than one wavelength ($\lambda = 5.7$ cm for 5.24 GHz signal), then the trajectory of the CSI ratio during respiration is just an arc (part of a full circle). As shown in Fig. 11.9, when a subject inhales and exhales during respiration, the length of the dynamic reflection path increases and decreases accordingly. The CSI ratio rotates along the arc clockwise or counterclockwise, corresponding to inhalation and exhalation, respectively. Note that the commodity WiFi card provides CSI on multiple sub-carriers, e.g., 30 sub-carriers for Intel 5300 card. We then apply the Savitzky–Golay filter [33] to smooth the CSI ratio data of each sub-carrier and use them for further processing.

As shown in Eq. (11.13), the amplitude noise and time-varying phase offset are effectively canceled out by the division operation. Apparently, compared to the raw CSI reading from a single antenna, the CSI ratio between two adjacent antennas contains less noise and is thus more sensitive in detecting weak reflection signals, leading to a longer sensing range. To extract respiration pattern from a time series of complex-valued CSI ratio data **x**, we linearly combine its

real part (I component) and imaginary part (Q component) by assigning weights $\cos\alpha$ and $\sin\alpha$ as:

$$\mathbf{y} = \begin{bmatrix} \cos\alpha & \sin\alpha \end{bmatrix} \begin{bmatrix} \Re(\mathbf{x}) & \Im(\mathbf{x}) \end{bmatrix}^T, \tag{11.16}$$

where $\Re(\mathbf{x})$ is the real part of $\mathbf{x}$ and $\Im(\mathbf{x})$ is the imaginary part of $\mathbf{x}$. By varying α from 0 to 2π at a fixed step size, we can generate various combination of candidates. The one that has the maximal periodicity is selected from these candidates following the method presented in [5]. Note that, as amplitude and phase are complementary to each other and when both of them are utilized, the number of "blind spots" is significantly reduced.

We further estimate respiration rate by combining results from multiple sub-carriers. First, for each sub-carrier, we calculate the autocorrelation of its respiration pattern, where the autocorrelation function describes the similarity of a signal to a shifted version of itself [34]. Second, we combine the sub-carriers by employing a weighted sum of each sub-carrier's autocorrelation result, where the weight of each sub-carrier is the respiration pattern's BNR value [5]. The first peak of the combined autocorrelation result is the component describing the periodicity of respiration. Also, the shift of the first peak divided by the sampling rate is the estimated period for one respiration cycle. Fig. 11.10 shows an example of respiration-rate estimation by combining multiple sub-carriers. Three sub-carriers (i.e., 4, 8, and 17) are selected to participate in the weighted sum operation. As shown in the final combined autocorrelation result, the lag (shift) of the first peak labeled with 1 is 335. For a sampling rate of 100 Hz, the estimated respiration rate is calculated as $\frac{60}{335/100} = 17.9$ bpm.

11.4.2.3 Evaluation

We employ a pair of GIGABYTE mini-PCs, each equipped with one Intel 5300 WiFi card as a transceiver. One antenna is employed at the transmitter (Tx), and two antennas are used at the receiver (Rx). The carrier frequency of the WiFi channel is set as 5.24 GHz, and the transmitter is set to broadcast 100 packets per second. We collect CSI data at the receiver using the CSI tool [10] and process it with MATLAB® at a DELL Precision 5520 laptop. We collect the ground-truth respiration rates of a human subject with a commercial device (Neulog Respiration Monitor Belt logger sensor NUL-236).

In the experiments, the human subject is instructed to sit or lie down facing the WiFi transceiver pair and breathe naturally. To demonstrate the effectiveness and robustness of the presented methods, we conduct experiments in three different scenarios:

1. Scenario 1: As shown in Fig. 11.11 (a), the human subject is located at various distances ranging –nine 9 m with respect to the WiFi transceivers placed at a height of one m in a large office room with a size of 7.5 m × 9 m;
2. Scenario 2: As shown in Fig. 11.11 (b), both WiFi transceivers are mounted on the ceiling, far away from the human subject;
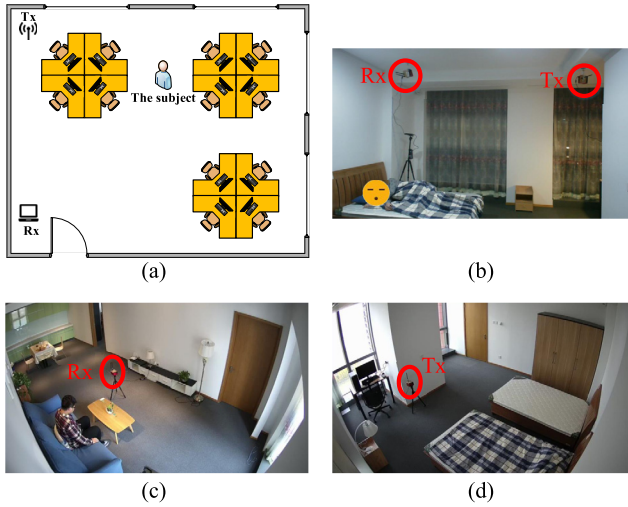
FIGURE 11.11 Experimental setup in three different environments: (a) sitting far away from the transceivers; (b) sleeping scenario; (c) and (d) NLoS scenario.
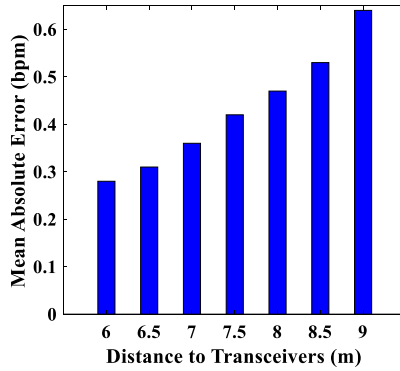

FIGURE 11.12 The mean absolute error of respiration rate vs. distance to transceivers.

3. Scenario 3: As shown in Fig. 11.11 (c) and (d), the WiFi transmitter and receiver are placed in two different rooms separated by a wall.

The experiment results are presented here:

1. We plot the mean absolute error of the respiration rate when the distance between the human subject and WiFi transceivers is increased from 4 m to 9 m in Fig. 11.12. As expected, the error increases with the distance. This is because the reflection signal is weaker when the distance is increased. Even when the distance is eight m, the mean absolute error is still less than 0.5 bpm. This result shows that the proposed method is able to achieve a sensing range of eight–nine m, large enough for house-level sens-
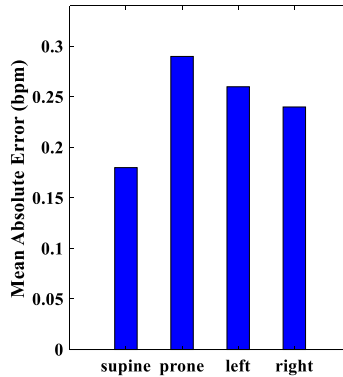
FIGURE 11.13 The mean absolute error of respiration rate vs. the sleeping postures.

    ing. In contrast, the traditional approaches have a much shorter sensing range (two–four m).

2. Fig. 11.13 shows the mean absolute error of the respiration rate for various sleeping postures. For all four postures (supine, prone, left, and right), the mean absolute error is always less than 0.3 bpm, which demonstrates the effectiveness and robustness of the proposed method. It can also be observed that the respiration rate is more accurate in a supine posture than in other postures. We believe this is because in a supine posture, the subject's chest faces the transceivers and therefore induces larger signal fluctuations compared to other postures.

3. For the challenging NLoS scenario with WiFi transmitter and receiver placed in two different rooms, the achieved mean absolute error is still as small as 0.34 bpm. The error at the same distance of five m for the NLoS scenario is slightly larger than that for the LoS scenario. This is because the signal reflected off the human subject becomes even weaker after penetrating the wall.

11.5 Robust multi-person respiration monitoring

11.5.1 Modeling of CSI-based multi-person respiration sensing

In this subsection, we show how to model multi-person respiration sensing with WiFi CSI.

11.5.1.1 Effects of multi-person respiration on WiFi CSI

Fig. 11.14 presents a typical WiFi-based multi-person respiration sensing scenario, where the Wi–Fi transceivers are placed at fixed locations and multiple persons are present breathing normally. In this scenario, the WiFi signals are affected by multiple targets simultaneously. Let's first study the effect of multi-
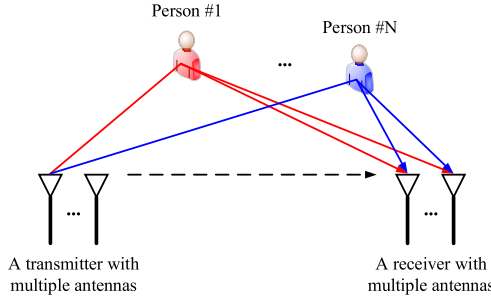
FIGURE 11.14 A typical WiFi-based multi-person respiration sensing scenario.

person respiration on WiFi CSI with just one transmitting antenna and one receiving antenna. Based on Eq. (11.1), we can represent the CSI in multi-person scenario as follows:

$$H(f,t) = \delta(t)e^{-j\phi(t)}\left(\sum_{i=1}^{N} A_i e^{-j\cdot 2\pi d_i(t)/\lambda} + b\right), \tag{11.17}$$

where $\delta(t)$ is the amplitude impulse noise, $\phi(t)$ is the time-varying phase offset, N is the number of persons to monitor, $d_i(t)$ is the path length of the signal bounced off the chest of the ith person, and b is the combined static signal. When the ith person breathes, the reflection path length $d_i(t)$ varies corresponding to his/her chest movement, and $H(f,t)$ changes accordingly. The key to achieve multi-person respiration sensing is to extract the respiration signal $e^{-j\cdot 2\pi d_i(t)/\lambda}$ corresponding to the respiration of each individual person from Eq. (11.17).

We now consider the scenario when multiple antennas are available at the WiFi transceivers. Two key observations identified in [5] help us derive the formula of CSI from various antenna pairs. First, for each person, with a tiny movement (e.g., a few millimeters), although the reflection path length obtained from each antenna pair (one at the transmitter and one at the receiver) changes, the path-length difference between two antenna pairs can be considered as a constant. Second, for commodity WiFi devices, the time-varying phase offsets in Eq. (11.17) are the same across different antennas at the same device since they share a same RF oscillator. With these two observations, we can denote the CSI readings from two different antenna pairs as follows:

$$\begin{cases} H_1(f,t) = \delta(t)e^{-j\phi(t)}(\sum_{i=1}^{N} A_{1,i}e^{-j2\pi\frac{d_{1,i}(t)}{\lambda}} + b_1) \\ H_2(f,t) = \delta(t)e^{-j\phi(t)}(\sum_{i=1}^{N}(A_{2,i}e^{-j2\pi\frac{d_{2,i}(t)-d_{1,i}(t)}{\lambda}})e^{-j2\pi\frac{d_{1,i}(t)}{\lambda}} + b_2), \end{cases} \tag{11.18}$$

where $H_1(f,t)$ is the CSI from one antenna pair, $H_2(f,t)$ is the CSI from another antenna pair, and $d_{2,i}(t) - d_{1,i}(t)$ is the path-length difference between two antenna pairs for the ith person, which is a constant.

11.5.1.2 Modeling multi-person respiration sensing as a blind-source separation problem

The goal of multi-person respiration sensing is to extract the source respiration signal $s_i(f, t) = e^{-j2\pi d_{1,i}(t)/\lambda}$ $(i = 1, 2, ..., N)$ corresponding to the respiration of each individual from Eq. (11.18). This is quite similar to the well-known blind-source separation (BSS) problem that aims to recover each individual source signal from a given mixed signal without knowing how they are mixed together [35]. In essence, the BSS problem can be efficiently solved by a technique called Independent Component Analysis (ICA), if three assumptions are satisfied [36]: (1) The signal sources are non-Gaussian; (2) the signal sources are mutually statistically independent; and (3) the mixture is of linear nature. All the three assumptions are satisfied in multi-person respiration sensing, and therefore the problem can be modeled as the BSS problem, and the source signals can be separated by the ICA method.

The basic ideal sounds promising. However, as shown in Eq. (11.18), it is noticed that the CSI readings obtained from commodity WiFi hardware suffer from amplitude noise $\delta(t)$ and time-varying phase offset $\phi(t)$. To apply the ICA method for WiFi-based multi-person respiration sensing, we need to eliminate the noise and random phase offset. To achieve this goal, we propose a novel signal-transformation technique, which contains two steps: (1) We construct a so-called "reference CSI" that has the same form as $H_0(f, t) = \delta(t)e^{-j\phi(t)}b_0$; and (2) for CSI $H_k(f, t)$ from the kth antenna pairs, we normalize it by the "reference CSI" as follows:

$$\frac{H_k(f,t)}{H_0(f,t)} = \frac{\delta(t)e^{-j\phi(t)}(\sum_{i=1}^{N} a_{k,i} s_i(f,t) + b_k)}{\delta(t)e^{-j\phi(t)}b_0} = \sum_{i=1}^{N} \frac{a_{k,i}}{b_0} s_i(f,t) + \frac{b_k}{b_0},$$

(11.19)

where $a_{k,i}$ is the coefficient of the respiration signal $s_i(f, t) = e^{-j2\pi d_{1,i}(t)/\lambda}$ in CSI collected from the kth antenna pair. We can clearly observe that the noise in original CSI is successfully canceled out by the signal transformation operation, while the linear mixture nature of WiFi CSIs are still kept.

To construct such a special "reference CSI", we employ a weighted sum of all CSI readings from M different antenna pairs as follows:

$$H_{sum}(f,t) = \sum_{k=1}^{M} g_k H_k(f,t)$$

$$= \delta(t)e^{-j\phi(t)}(\sum_{i=1}^{N}\sum_{k=1}^{M} a_{k,i} g_k s_i(f,t) + \sum_{k=1}^{M} g_k b_k),$$

(11.20)

where M is the number of antenna pairs, N is the number of persons, and g_k $(k = 1, 2, ..., M)$ is the weight. Mathematically, the "reference CSI" can be obtained

from Eq. (11.20):

$$H_{ref}(f,t) = \delta(t)e^{-j\phi(t)} \sum_{k=1}^{M} g_k b_k, \qquad (11.21)$$

if the following condition is satisfied:

$$\begin{cases} \sum_{k=1}^{M} a_{k,1} g_k = 0 \\ \sum_{k=1}^{M} a_{k,2} g_k = 0 \\ \quad\vdots \\ \sum_{k=1}^{M} a_{k,N} g_k = 0 \end{cases} \qquad (11.22)$$

Obviously, Eq. (11.22) is an homogeneous system of linear equations that has N equations and M variables ($g_1, g_2, ..., g_M$). Given that $M > N$, there must be some nontrivial solutions to satisfy Eq. (11.22).

In practice, we apply the genetic algorithm to search for such a solution by minimizing the RER (Respiration Energy Ratio) of $H_{sum}(f,t)$, where the RER is defined as the ratio of respiration-related energy to the total signal energy [24]. We subtract the background CSI measured when there is no target in the environment. In this way, the CSI after signal transformation is exactly the linear mixture of the respiration signal of each person, and the ICA method can then be applied to separate the source signal $s_i(f,t) = e^{-j2\pi d_{1,i}(t)/\lambda}$. After that, we extract the respiration pattern of each individual target from the complex-valued signal by applying the Principle Component Analysis (PCA) method presented in [37]. The respiration rate can be estimated by counting the peaks in a specific window of respiration signals using the method proposed in [4].

11.5.2 The advantages of our approach

In this subsection, we will explain why our approach outperforms the existing approaches that rely on the spectral analysis of the CSI amplitude.

11.5.2.1 Reducing the noise in CSI amplitude

As shown in Eq. (11.22), most of the noise in CSI amplitude is canceled out by the division operation. Compared to the original CSI amplitude, the proposed new signal ratio has a higher SNR (Signal-to-Noise Ratio), which is thus more sensitive in detecting subtle respiration-induced chest displacement.

11.5.2.2 Eliminating the "blind spots"

Now, we explain why the "blind spots" do not exist in our systems. In multi-person scenarios, the signals reflected from multiple persons are mixed together in the CSI. When the complex-valued CSI is projected to its real-valued amplitude, for each respiration signal, different projection axes have different capabil-

FIGURE 11.15 The experimental setup in two scenarios: (a) All subjects are sleeping on a bed; (b) each subject is sitting on a couch or chair.

ities in terms of sensing respiration [24]. Traditional approaches simply project the complex-valued CSI into its amplitude, thus all respiration signals share the same project axis. However, a good projection axis for the respiration signal of one person may be a bad one for that of another person, thus resulting in the "blind spots" issue. In contrast to prior work that projects the mixed respiration signals onto one axis, our approach separates the respiration signals of multiple persons and projects each respiration signal on its unique best axis to extract the respiration pattern. Therefore, the "blind spots" issue is well-addressed.

11.5.2.3 Resolving similar respiration rates

Based on the literature on blind-source separation, our approach can efficiently extract the source respiration signals as long as they are mutually independent of each other. Such condition holds true even when two persons have similar respiration rates. This is because breathing is a natural physical activity and two persons' respiration processes have an extremely small chance to be fully synchronized over time. In other words, two people might have similar respiration rates but generally with different phases.

11.5.3 Evaluation

11.5.3.1 Experimental setup

We use two GigaByte mini-PCs equipped with Intel 5300 WiFi cards as transceivers. Both the transmitter and receiver are equipped with three omnidirectional antennas. The frequency of WiFi channel is set to 5.24 GHz with a bandwidth of 20 MHz. The transmitter sends 200 packets per sec at a transmission power of 15 dBm. We collect CSI data at the receiver using the CSI tool [10] and process it with MATLAB on a DELL Precision 5520 laptop in real time. To obtain the ground-truth respiration of multiple persons, we ask each of them to wear a commercial Neulog respiration belt.
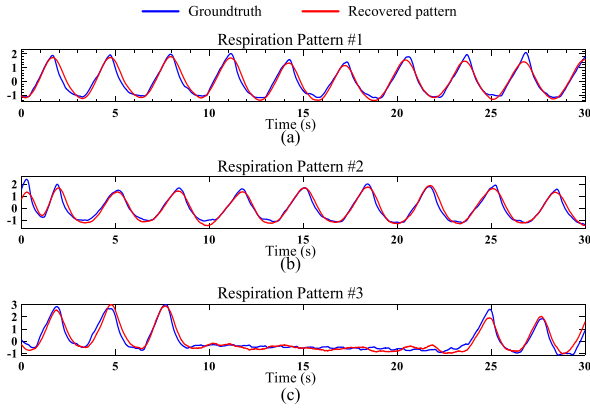
FIGURE 11.16 An example of detected respiration patterns and the ground-truth patterns in a three-person scenario.

In our experiments, each of the human subjects is instructed to sit or lie down facing the WiFi transceiver pair and breathe naturally. We recruited 21 participants, i.e., 12 males and 9 females, aged from 14 to 57. Their natural respiration rates range from 14 bpm to 22 bpm. To demonstrate the effectiveness and robustness of the proposed system, we conduct experiments in two different environments:

1. Environment 1: As shown in Fig. 11.15 (a), multiple subjects are sleeping on a bed with a size of 1.9 m × 2.4 m in a bedroom;
2. Environment 2: As shown in Fig. 11.15 (b), multiple subjects are sitting in a couch or chair in a living room with a size of 4 m × 7.5 m.

Both environments are equipped with furniture and electrical appliances, which create rich multipaths. For the sleeping scenario in Fig. 11.15 (a), we mount the transceivers on the ceiling with a spacing of 2.7 m between them. For the sitting scenario in Fig. 11.15 (b), we place the transceivers on two tripods.

11.5.3.2   Experiment results

The experiment results are presented using multi-person scenario as examples, detailed respiration patterns, and the mean absolute respiration-rate errors will be reported:

1. Fig. 11.16 shows three detected respiration patterns and the corresponding ground-truth patterns when three persons sit on the couch. From Fig. 11.16(a) and Fig. 11.16(b), we can see that the proposed method is able to separate two respiration patterns even when they are very similar to each other. Fig. 11.16(c) shows that the proposed method can correctly detect irregular respiration patterns caused by health issues such as apnea that occur in the time interval from the 9th to 22nd second.
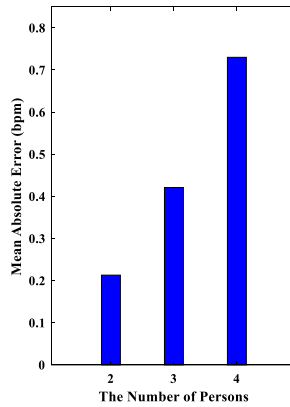
FIGURE 11.17 The mean absolute respiration rate error vs. the number of persons.

2. We plot the mean absolute errors of respiration rate for two-person, three-person, four-person, and five-person scenarios in Fig. 11.17. The results show that the mean absolute error is 0.21 bpm for the two-person scenario and it increases to 0.42 bpm for the three-person scenario. Please note that a larger than 1-bpm error is usually unacceptable for respiration monitoring. For the four-person scenario, the proposed method can still achieve an error of 0.73 bpm. However, in the five-person scenario, an error larger than 1 bpm is observed. As expected, the error increases with the number of persons monitored. The experiment results demonstrate the effectiveness and robustness of the proposed method for respiration monitoring in two-person, three-person, and four-person scenarios.

11.6 Summary

In this chapter, we first provide a historical review of WiFi-based contact-free human respiration monitoring solutions, and then we introduce the Fresnel reflection and diffraction model to show how human respiration monitoring can be achieved by using WiFi signals. To address the problem of "blind spots" and limited sensing range, we propose a series of solutions including exploiting the complementary property of amplitude and phase, adding "virtual" multipath, and creating a new base signal called CSI ratio. We further leverage multiple antennas available in commodity WiFi cards to achieve accurate multi-person respiration sensing for the first time.

While great progress has been made in WiFi-based respiration sensing, several challenges still need to be addressed in future work, such as how to robustly monitor human respiration when the targets are moving, and how to ensure the robustness of human respiration sensing performance when the targets are in different locations and orientations.

Acknowledgments

References

[1] A.N. Pedersen, S. Korreman, H. Nyström, L. Specht, Breathing adapted radiotherapy of breast cancer: reduction of cardiac and pulmonary doses using voluntary inspiration breath-hold, Radiotherapy and Oncology 72 (1) (2004) 53–60.

[2] X. Liu, J. Cao, S. Tang, J. Wen, P. Guo, Contactless respiration monitoring via off-the-shelf wifi devices, IEEE Transactions on Mobile Computing 15 (10) (2015) 2466–2479.

[3] H. Wang, D. Zhang, J. Ma, Y. Wang, Y. Wang, D. Wu, T. Gu, B. Xie, Human respiration detection with commodity wifi devices: do user location and body orientation matter?, in: Proceedings of the 2016 ACM International Joint Conference on Pervasive and Ubiquitous Computing, 2016, pp. 25–36.

[4] Y. Zeng, D. Wu, R. Gao, T. Gu, D. Zhang, Fullbreathe: full human respiration detection exploiting complementarity of csi phase and amplitude of wifi signals, Proceedings of the ACM on Interactive, Mobile, Wearable and Ubiquitous Technologies 2 (3) (2018) 1–19.

[5] Y. Zeng, D. Wu, J. Xiong, E. Yi, R. Gao, D. Zhang, Farsense: pushing the range limit of wifi-based respiration sensing with csi ratio of two antennas, Proceedings of the ACM on Interactive, Mobile, Wearable and Ubiquitous Technologies 3 (3) (2019) 1–26.

[6] N. Patwari, J. Wilson, S. Ananthanarayanan, S.K. Kasera, D.R. Westenskow, Monitoring breathing via signal strength in wireless networks, IEEE Transactions on Mobile Computing 13 (8) (2013) 1774–1786.

[7] O. Kaltiokallio, H. Yiğitler, R. Jäntti, N. Patwari, Non-invasive respiration rate monitoring using a single cots tx-rx pair, in: IPSN-14 Proceedings of the 13th International Symposium on Information Processing in Sensor Networks, IEEE, 2014, pp. 59–69.

[8] H. Abdelnasser, K.A. Harras, M. Youssef, Ubibreathe: a ubiquitous non-invasive wifi-based breathing estimator, in: Proceedings of the 16th ACM International Symposium on Mobile Ad Hoc Networking and Computing, 2015, pp. 277–286.

[9] E. Perahia, R. Stacey, Next Generation Wireless LANs: 802.11 n and 802.11 ac, Cambridge University Press, 2013.

[10] D. Halperin, W. Hu, A. Sheth, D. Wetherall, Tool release: gathering 802.11 n traces with channel state information, ACM SIGCOMM Computer Communication Review 41 (1) (2011) 53.

[11] X. Liu, J. Cao, S. Tang, J. Wen, Wi-sleep: contactless sleep monitoring via wifi signals, in: 2014 IEEE Real-Time Systems Symposium, IEEE, 2014, pp. 346–355.

[12] J. Liu, Y. Wang, Y. Chen, J. Yang, X. Chen, J. Cheng, Tracking vital signs during sleep leveraging off-the-shelf wifi, in: Proceedings of the 16th ACM International Symposium on Mobile Ad Hoc Networking and Computing, 2015, pp. 267–276.

[13] C. Wu, Z. Yang, Z. Zhou, X. Liu, Y. Liu, J. Cao, Non-invasive detection of moving and stationary human with wifi, IEEE Journal on Selected Areas in Communications 33 (11) (2015) 2329–2342.

[14] D. Wu, D. Zhang, C. Xu, H. Wang, X. Li, Device-free wifi human sensing: from pattern-based to model-based approaches, IEEE Communications Magazine 55 (10) (2017) 91–97.

[15] D. Zhang, H. Wang, D. Wu, Toward centimeter-scale human activity sensing with wi-fi signals, Computer 50 (1) (2017) 48–57.

[16] F. Zhang, D. Zhang, J. Xiong, H. Wang, K. Niu, B. Jin, Y. Wang, From Fresnel diffraction model to fine-grained human respiration sensing with commodity wi-fi devices, Proc. ACM Interact. Mob. Wearable Ubiquitous Technol. 2 (1) (2018) 53:1–53:23.

[17] K. Niu, F. Zhang, J. Xiong, X. Li, E. Yi, D. Zhang, Boosting fine-grained activity sensing by embracing wireless multipath effects, in: Proceedings of the 14th International Conference on Emerging Networking EXperiments and Technologies, 2018, pp. 139–151.

[18] P. Wang, B. Guo, T. Xin, Z. Wang, Z. Yu Tinysense, Multi-user respiration detection using wi-fi csi signals, in: 2017 IEEE 19th International Conference on e-Health Networking, Applications and Services (Healthcom), IEEE, 2017, pp. 1–6.

[19] X. Wang, C. Yang, S. Mao, Phasebeat: exploiting csi phase data for vital sign monitoring with commodity wifi devices, in: 2017 IEEE 37th International Conference on Distributed Computing Systems (ICDCS), IEEE, 2017, pp. 1230–1239.

[20] B.D. Rao, K.S. Hari, Performance analysis of root-music, IEEE Transactions on Acoustics, Speech, and Signal Processing 37 (12) (1989) 1939–1949.

[21] C. Chen, Y. Han, Y. Chen, H.-Q. Lai, F. Zhang, B. Wang, K.R. Liu, Tr-breath: time-reversal breathing rate estimation and detection, IEEE Transactions on Biomedical Engineering 65 (3) (2017) 489–501.

[22] X. Wang, C. Yang, S. Mao Tensorbeat, Tensor decomposition for monitoring multiperson breathing beats with commodity wifi, ACM Transactions on Intelligent Systems and Technology (TIST) 9 (1) (2017) 1–27.

[23] Y. Yang, J. Cao, X. Liu, K. Xing, Multi-person sleeping respiration monitoring with cots wifi devices, in: 2018 IEEE 15th International Conference on Mobile Ad Hoc and Sensor Systems (MASS), IEEE, 2018, pp. 37–45.

[24] Y. Zeng, D. Wu, J. Xiong, J. Liu, Z. Liu, D. Zhang, Multisense: enabling multi-person respiration sensing with commodity wifi, Proceedings of the ACM on Interactive, Mobile, Wearable and Ubiquitous Technologies 4 (3) (2020) 1–29.

[25] S. Shi, Y. Xie, M. Li, A.X. Liu, J. Zhao, Synthesizing wider wifi bandwidth for respiration rate monitoring in dynamic environments, in: IEEE INFOCOM 2019-IEEE Conference on Computer Communications, IEEE, 2019, pp. 181–189.

[26] D. Zhang, Y. Hu, Y. Chen, B. Zeng, Breathtrack: tracking indoor human breath status via commodity wifi, IEEE Internet of Things Journal 6 (2) (2019) 3899–3911.

[27] P. Hillyard, A. Luong, A.S. Abrar, N. Patwari, K. Sundar, R. Farney, J. Burch, C. Porucznik, S.H. Pollard, Experience: cross-technology radio respiratory monitoring performance study, in: Proceedings of the 24th Annual International Conference on Mobile Computing and Networking, 2018, pp. 487–496.

[28] W. Wang, A.X. Liu, M. Shahzad, K. Ling, S. Lu, Understanding and modeling of wifi signal based human activity recognition, in: Proceedings of the 21st Annual International Conference on Mobile Computing and Networking, MobiCom'15, Association for Computing Machinery, New York, NY, USA, 2015, pp. 65–76.

[29] C. Lowanichkiattikul, M. Dhanachai, C. Sitathanee, S. Khachonkham, P. Khaothong, Impact of chest wall motion caused by respiration in adjuvant radiotherapy for postoperative breast cancer patients, SpringerPlus 5 (1) (2016) 1–8.

[30] A.F. Molisch, Wireless communications, John Wiley and Sons, Chichester, UK.

[31] M. Kotaru, K. Joshi, D. Bharadia, S. Katti, Spotfi: decimeter level localization using wifi, in: Proceedings of the 2015 ACM Conference on Special Interest Group on Data Communication, 2015, pp. 269–282.

[32] H. Schwerdtfeger, Geometry of Complex Numbers: Circle Geometry, Moebius Transformation, Non-euclidean Geometry, Courier Corporation, 1979.

[33] K. Baba, L. Bahi, L. Ouadif, Enhancing geophysical signals through the use of Savitzky-Golay filtering method, Geofísica Internacional 53 (4) (2014) 399–409.

[34] G.E. Box, G.M. Jenkins, G.C. Reinsel, G.M. Ljung, Time Series Analysis: Forecasting and Control, John Wiley & Sons, 2015.

[35] F. Abrard, Y. Deville, A time–frequency blind signal separation method applicable to underdetermined mixtures of dependent sources, Signal Processing 85 (7) (2005) 1389–1403.

[36] V.D. Sánchez A, Frontiers of research in bss/ica, Neurocomputing 49 (1–4) (2002) 7–23.

[37] A.D. Droitcour, et al., Non-contact measurement of heart and respiration rates with a single-chip microwave Doppler radar, Ph.D. thesis, Citeseer, 2006.